

# Boundary Scattering in Ballistic Graphene

Satoru Masubuchi,<sup>1,2,\*</sup> Kazuyuki Iguchi,<sup>1</sup> Takehiro Yamaguchi,<sup>1</sup> Masahiro Onuki,<sup>1</sup>  
Miho Arai,<sup>1</sup> Kenji Watanabe,<sup>3</sup> Takashi Taniguchi,<sup>3</sup> and Tomoki Machida<sup>1,2,4,†</sup>

<sup>1</sup>*Institute of Industrial Science, University of Tokyo,  
4-6-1 Komaba, Meguro-ku, Tokyo 153-8505, Japan.*

<sup>2</sup>*Institute for Nano Quantum Information Electronics,  
University of Tokyo, 4-6-1 Komaba, Meguro-ku Tokyo 153-8505, Japan.*

<sup>3</sup>*National Institute for Materials Science,  
1-1 Namiki, Tsukuba, 305-0044, Japan.*

<sup>4</sup>*PRESTO-JST, 4-1-8 Honcho, Kawaguchi, Saitama 332-0012, Japan*

## Abstract

We report magnetotransport measurements in ballistic graphene/hexagonal boron nitride mesoscopic wires where the charge carrier mean free path is comparable to wire width  $W$ . Magnetoresistance curves show characteristic peak structures where the peak field scales with the ratio of cyclotron radius  $R_c$  and wire width  $W$  as  $W/R_c = 0.9 \pm 0.1$ , due to diffusive boundary scattering. The obtained proportionality constant between  $R_c$  and  $W$  differs from that of a classical semiconductor 2D electron system where  $W/R_c = 0.55$ .

<sup>11</sup> PACS numbers: 72.80.Vp

<sup>12</sup> Keywords: graphene, hexagonal boron nitride, ballistic transport, magnetoresistance

13 The presence of unique relativistic charge carriers, massless Dirac fermions, in monolayer  
14 graphene [1] has led to the emergence of novel transport phenomena such as half-integer  
15 [2, 3] and fractional quantum Hall effect [4, 5]. When the elastic mean free path of Dirac  
16 fermions becomes comparable to the sample size, the charge carrier transport mechanism  
17 enters a quasi-ballistic regime [6], and Dirac fermions exhibit more intriguing relativistic  
18 transport phenomena such as Klein tunneling [7], evanescent wave transport [8], and sub-  
19 Poissonian shot noise [9]. In quasi-ballistic graphene devices, the probability of charge  
20 carrier scattering at sample boundaries becomes significantly larger than in the bulk region,  
21 because the probabilities of charge carriers scattering from charged impurities [10], defects  
22 [11], longitudinal acoustic phonons [12, 13], substrate optical phonons [12, 14], and flexural  
23 phonons [15] are significantly suppressed. To understand the fundamental transport proper-  
24 ties of quasi-ballistic graphene, it is highly desirable to characterize the effects of boundary  
25 scattering.

26 In the mesoscopic wire system made from conventional semiconductor-based two-dimensional  
27 electron systems, it has been established that, if the charge carriers travel ballistically in  
28 the bulk region and are scattered diffusively at the sample boundary, the device exhibits  
29 anomalous magnetoresistance peaks owing to the magnetic commensurability effect between  
30 cyclotron radius  $R_c$  and wire width  $W$  [6, 16]. Moreover, since the anomalous magnetore-  
31 sistance peaks are due to diffuse boundary scattering, the probability of specular scattering,  
32 namely specularity parameter  $p$ , can be extracted by measuring anomalous magnetoresis-  
33 tance peaks [16–19].

34 Recent development of a transfer technique of graphene on hexagonal boron nitride (h-  
35 BN) [20, 21] have made a breakthrough in the studies of ballistic transport phenomena  
36 in graphene [22]. Since the surface of h-BN is atomically flat and h-BN has high optical  
37 phonon energy as compared to SiO<sub>2</sub>, graphene on h-BN exhibits extraordinary high mobility  
38  $\mu \sim 100,000$  cm<sup>2</sup>/Vs and a long mean free path  $l_{\text{mfp}} = (h/2e)\mu\sqrt{n/\pi} \sim 1$   $\mu\text{m}$  [22, 23]. In  
39 conventional graphene on SiO<sub>2</sub> devices,  $\mu$  is relatively low, and  $l_{\text{mfp}}$  is limited to 100 nm [12].  
40 Suspended graphene devices show high  $\mu = 200,000$  cm<sup>2</sup>/Vs [24, 25], but the observation of  
41 boundary scattering effect has not been reported [26].

42 In this letter, we report on magnetotransport measurements in ballistic graphene/hexagonal  
43 boron nitride mesoscopic wires, in which the carrier mean free path is comparable to the  
44 wire width. We observed anomalous magnetoresistance curves with characteristic peak

45 structures where the peak field scales with the ratio of cyclotron radius  $R_c$  and wire width  
 46  $W$  as  $W/R_c = 0.9 \pm 0.1$ , which indicates the detection of diffusive charge carrier scattering at  
 47 the graphene boundary. The obtained proportionality constant between  $R_c$  and  $W$  contrasts  
 48 that of the classical semiconductor two-dimensional electron system, in which  $W/R_c = 0.55$ .  
 49 In addition, from the analysis of magnetoresistance amplitude, nearly zero specularly at  
 50 the graphene boundary is suggested.

51 The graphene/hexagonal boron nitride (GBN) mesoscopic wire system was fabricated  
 52 using the following lithography steps [20, 27–29]. First, relatively thick h-BN crystals ( $\sim 10$   
 53 nm) were deposited on a Si wafer using a mechanical exfoliation technique. A monolayer  
 54 graphene flake was deposited on a spin-coated polymethylmethacrylate (PMMA) layer and  
 55 transferred on a h-BN crystal using an alignment technique under an optical microscope [20].  
 56 Monolayer thickness of a graphene flake was verified by Raman spectroscopy. Bar-shaped  
 57 geometry was defined using standard electron-beam lithography and subsequent oxygen  
 58 plasma etching. The electrical contacts were defined by electron-beam lithography followed  
 59 by the evaporation of Pd (80 nm) and lift-off. The resist residues were removed by annealing  
 60 at 300 °C in Ar/H<sub>2</sub> (97:3) gas flow for 6 h.

61 In order to study the dependence of the transport properties on channel length  $L$ , we  
 62 fabricated three devices for  $L = 0.6, 1.4, \text{ and } 2.3 \mu\text{m}$  with channel width  $W = 1.0 \mu\text{m}$  in a  
 63 single graphene flake [inset in Fig. 1(a)]. Transport measurements were carried out using  
 64 the standard lock-in technique with a small alternating current of  $I_{ac} = 100 \text{ nA}$  in a variable  
 65 temperature insert at  $T = 1.5 \sim 300 \text{ K}$ . A heavily doped Si substrate was used as a global  
 66 back gate  $V_g$  to tune carrier density  $n = C_g(V_g - V_{\text{Dirac}})$ , where  $C_g = 1.07 \times 10^{-4} \text{ F/m}^2$  is the  
 67 gate capacitance and  $V_{\text{Dirac}}$  is the value of  $V_g$  at the charge neutrality point [2]. A magnetic  
 68 field was applied perpendicularly to the sample surface.

69 Figure 1(a) shows conductivity  $\sigma$  as a function of  $V_g$  for the  $L = 2.3 \mu\text{m}$  device measured  
 70 at  $T = 4, 16, 60, 120, 180, 240, \text{ and } 300 \text{ K}$  (from top to bottom). To extract conductivity  $\sigma$   
 71 from the measured resistance, the contribution of contact resistance were eliminated using  
 72 transfer length method [supplementary information]. Typical V-shaped dependence of  $\sigma$   
 73 on  $V_g$  was observed for all temperatures. Minimum conductivity was located close to zero-  
 74 gate bias voltages  $V_{\text{Dirac}} \sim -0.3 \text{ V}$ , indicating small unintentional doping ( $\sim 10^{10} \text{ cm}^{-2}$ ).  
 75 The carrier mobility limited by long-range scattering (described below) on hole side reached  
 76  $\mu_1 = 63,000 \text{ cm}^2/\text{Vs}$  at  $T = 4 \text{ K}$ . In the following discussions, we focus on the hole side of

77 the  $\sigma$  because the hole mobility was higher than the electron mobility.

78 To extract the mean free path, we fitted the conductivity using the transport formula  
 79 and assuming long- and short-range scattering as the major contributors to charge carrier  
 80 scattering [30, 31],  $\sigma^{-1} = (ne\mu_l)^{-1} + \rho_s$ , where  $\mu_l$  is the mobility from long-range scattering,  
 81 and  $\rho_s$  is the resistivity from short-range scattering, which are both independent of charge  
 82 carrier density  $n$  [20]. In  $-35 \text{ V} < V_g < 0 \text{ V}$ , the experimental data are well fitted to the  
 83 calculated conductivity [dashed curve in Fig. 1(a)]. In  $-50 \text{ V} < V_g < -35 \text{ V}$ , the calculated  
 84 conductivity deviates from the experimental data. This deviation can indicate the presence  
 85 of an additional scattering mechanism, which is neither long- nor short-range scattering.

86 From the obtained values of  $\mu_l$  and  $\rho_s$  for varying temperatures  $T$ , we evaluated the  
 87 mean free path for long-range scattering  $l_{\text{long}} = \hbar\sqrt{n\pi}\mu_l e^{-1}$  and the mean free path for  
 88 short-range scattering  $l_{\text{short}} = \hbar\sqrt{\pi n^{-1}}\rho_s^{-1}e^{-2}$  [31]. The values of  $l_{\text{long}}$  and  $l_{\text{short}}$  as a function  
 89 of  $V_g$  for  $T = 4, 16, 60, 120, 180, 240,$  and  $300 \text{ K}$  are shown in Figs. 1(b) and (c) (from top  
 90 to bottom). The value of  $l_{\text{long}}$  increased with  $|V_g|$  [Fig. 1(b)], whereas the value of  $l_{\text{short}}$   
 91 decreased with  $|V_g|$  [Fig. 1(c)]. As the temperature increased, both  $l_{\text{long}}$  and  $l_{\text{short}}$  decreased.  
 92 These observations were qualitatively consistent with the previous transport measurements  
 93 in graphene on  $\text{SiO}_2$ . Quantitatively, however, the obtained values of  $l_{\text{long}} \sim 1.2 \mu\text{m}$  and  
 94  $l_{\text{short}} \sim 2 \mu\text{m}$  for  $V_g = -45 \text{ V}$  were substantially larger than the typical values in graphene on  
 95  $\text{SiO}_2$ , which were around hundred-nanometer range [12]; moreover, these values were larger  
 96 than sample width  $W$ .

97 Figure 2(a) shows two-terminal resistance  $R$  as a function of magnetic field  $B$  at  $V_g = -45$   
 98  $\text{V}$  and  $T = 4 \text{ K}$  for the  $L = 2.3 \mu\text{m}$  and  $W = 1.0 \mu\text{m}$  device. As we increased  $B$  from zero,  $R$   
 99 increased with  $B$  and exhibited a maximum at  $B_{\text{max}} = \pm 0.21 \text{ T}$ . As  $B$  was further increased,  
 100  $R$  decreased with  $B$  and exhibited a minimum at  $B_{\text{min}} = \pm 0.51 \text{ T}$ . For larger  $B$ ,  $R$  oscillated  
 101 as a function of  $B$ , which can be attributed to Shubnikov-de Haas oscillation.

102 In standard theory for ballistic transport phenomena in two-dimensional electron systems  
 103 in a small magnetic field [6], if the cyclotron radius is larger than the sample width,  $R_c > W$ ,  
 104 and if the electrons are scattered diffusively at the sample boundary, the boundary scattering  
 105 effect leads to an increase in the backscattering probability as schematically shown by solid  
 106 curves in the inset of Fig. 2(a). When the magnetic field is increased, the cyclotron diameter  
 107 becomes smaller than the sample width  $2R_c < W$ . Under this condition, a skipping orbit of  
 108 charge carriers at the sample boundary is formed, and the backscattering probability is sup-

109 pressed as schematically shown by the dashed curves in the inset of Fig. 2(a). Moreover, for  
 110 this condition, the quantization of the cyclotron orbit, i.e., Landau quantization, is allowed  
 111 because  $2R_c < W$ , thus Shubnikov-de Haas oscillation can be observed. The observation  
 112 of anomalous peak structures and Shubnikov-de Haas oscillation in Fig. 2 is thus qualita-  
 113 tively consistent with the expectations from the ballistic transport with diffusive boundary  
 114 scattering in the mesoscopic wire system [32].

115 We studied  $R$  as a function of  $B$  for shorter channel lengths of  $L = 1.4$  and  $0.6 \mu\text{m}$   
 116 [Fig. 2(b)]. The amplitude of anomalous magnetoresistance curve,  $\Delta R = R_{\text{max}} - R_{\text{min}}$   
 117 [indicated by solid and dotted arrows in Fig. 2(a), respectively], decreased with decreasing  
 118 channel length  $L$  [Fig. 2(c)]. In standard theory for diffusive boundary scattering, the  
 119 amplitude of anomalous magnetoresistance peaks is expected to decrease with  $L$ , because the  
 120 probability of back scattering decreases. Therefore, the observed decrease in the amplitude  
 121 of magnetoresistance peaks for  $L = 1.4$  and  $0.6 \mu\text{m}$  devices is also consistent with the  
 122 expectations from boundary scattering in the mesoscopic wire system. From the observations  
 123 in Fig. 2, it can be concluded that we have observed magnetoresistance peak structures due  
 124 to diffusive boundary scattering in a ballistic graphene mesoscopic wire system.

125 For quantitative understanding of the observed magnetoresistance curves, we discuss  
 126 here the positions of magnetoresistance peaks  $B_{\text{max}}$ . For diffusive boundary scattering,  
 127 the value of  $B_{\text{max}}$  scales with the ratio of cyclotron radius  $R_c(B, n)$  to the channel width  
 128  $W$  as  $W/R_c(B, n) = \alpha$ , where  $\alpha$  is the proportionality constant. For Dirac fermions in  
 129 monolayer graphene, the cyclotron radius can be written as  $R_c(B, n) = \frac{\hbar}{eB} \sqrt{\pi n}$ , where  $e$   
 130 is an elementary charge and  $\hbar$  is Planck's constant. Therefore, the expected positions of  
 131 resistance peaks in graphene can be expressed as

$$B_{\text{max}} = \alpha \frac{\hbar \sqrt{\pi n}}{e W} \quad (1)$$

132 To study the relationship between  $R_c$  and  $W$ , we measured magnetoresistance curves at  
 133 varying gate-bias voltages for the sample with  $(L, W) = (2.3 \mu\text{m}, 1.0 \mu\text{m})$ . Fig. 3(a) shows  
 134 two-terminal resistance  $R$  as a function of magnetic field  $B$  at  $V_g = -50, -48, \dots, -28 \text{ V}$   
 135 (bottom to top). In this plot, each curve was offset vertically so that peak positions were  
 136 separated by  $0.01 \text{ k}\Omega$ . At  $V_g = -50 \text{ V}$  (bottom curve), we observed the anomalous peak  
 137 structures at  $B_{\text{max}} = \pm 0.21 \text{ T}$ . As we increased gate-bias  $V_g$ , the positions of peak structures  
 138 were shifted to smaller  $B$ . At  $V_g = -28 \text{ V}$  (top curve), the peak positions were located at

139  $B_{\max} = \pm 0.14$  T. The peak positions were compared with the calculated  $B_{\max}$  using equation  
 140 (1). As shown by the colored areas in Fig. 3(a), the peak positions were well fitted with the  
 141 calculated positions for  $\alpha = 0.9 \pm 0.1$ .

142 To investigate the dependence of  $\alpha$  on the channel width, we studied another sample for  
 143 larger channel width  $(L, W) = (3.1 \mu\text{m}, 1.5 \mu\text{m})$  [Fig. 3(b)]. Compared with the device  
 144 with smaller  $W$  [Fig. 3(a)], the values of  $B_{\max}$  were decreased [Fig. 3(b)]. Moreover, the  
 145 peak positions were also fitted by the equation (1) for  $\alpha = 0.9 \pm 0.1$ , as indicated by the  
 146 colored area in Fig. 3(b). These analysis were also valid for other samples for  $(L, W) = (1.4$   
 147  $\mu\text{m}, 1.0 \mu\text{m})$  and  $(2.5 \mu\text{m}, 0.95 \mu\text{m})$ . These observations indicate the independence of the  
 148 proportionality constant  $\alpha$  on channel width  $W$ .

149 The obtained proportionality constant  $\alpha$  was larger than that of classical massive charge  
 150 carriers in the conventional semiconductor two-dimensional electron system (2DES) where  
 151  $\alpha = 0.55$  [16]. For comparison, we plot the expected positions of peak structures for  $\alpha = 0.55$   
 152 (blue curve) in Figs. 3(a) and 3(b). The curves for  $\alpha = 0.55$  could not explain the position  
 153 of peak structures. The conventional proportionality constant between  $R_c$  and  $W$  has to be  
 154 modified to explain the observed transport phenomena in graphene.

155 The differing value of  $W/R_c$  for graphene compared to that of conventional semiconductor  
 156 2DES indicate that the scattering process of massless Dirac fermions at sample boundaries  
 157 can be different from that of conventional 2DEGs. As a possible explanation for the differing  
 158 values of  $W/R_c$ , the interference of charge carriers at sample boundaries can be pointed out  
 159 [33]. Since the charge carriers in graphene are chiral, when the charge carrier scattering  
 160 at sample boundaries changes the momentum, the phase of their wave function are shifted.  
 161 This phase shift of wave function at sample boundaries induces complex interference of  
 162 charge carriers, which can alter the transport properties of ballistic graphene [33]. Moreover,  
 163 the first-principle numerical calculations of the magnetoresistance in graphene nanoribbon  
 164 suggested  $W/R_c = 0.8 - 1.0$  [34], which seems be consistent with our results. Albeit, for the  
 165 exact understandings of the reason for the differing values of  $W/R_c$ , more elaborated works  
 166 will be needed in the future.

167 Finally, we study the magnetoresistance curves for varying temperatures  $T$  and gate-bias  
 168 voltages  $V_g$ . Fig. 4(a) shows the amplitude of magnetoresistance  $\Delta R$ , long-range mean free  
 169 path  $l_{\text{long}}$ , and short-range mean free path  $l_{\text{short}}$  as a function of  $T$  at  $V_g = -35$  V. As  $T$  was  
 170 increased from 4 K to 240 K, the value of  $\Delta R$  was decreased, but was retained to  $T = 240$

171 K [Fig. 4(b)]. This observation implies that the channel region of graphene mesoscopic wire  
172 was still ballistic at  $T = 240$  K, because of the relatively small electron-phonon scattering  
173 probability in monolayer graphene compared to that of conventional semiconductors [12],  
174 which demonstrate the characteristic electronic properties of graphene.

175 Fig. 4(b) shows  $\Delta R$ ,  $l_{\text{long}}$ , and  $l_{\text{short}}$  as a function of  $V_g$  at  $T = 4$  K. The value of  $\Delta R$   
176 increased with  $|V_g|$  from 20 to 40 V and saturated for 40 to 50 V [Fig. 4(b)]. In principle,  
177  $\Delta R$  increases with the mean free path in the bulk region, and  $\Delta R$  saturates as the mean  
178 free path in the bulk region exceeds the sample width [6]. In Fig. 4(b), as we increased  
179  $|V_g|$ ,  $l_{\text{long}}$  increased, and for  $40 \text{ V} < |V_g| < 50 \text{ V}$ ,  $l_{\text{long}}$  exceeded the sample width [indicated  
180 by the dotted line in Fig. 4(b)]. On the other hand,  $l_{\text{short}}$  was decreased with  $|V_g|$  and  
181 were larger than  $W$ . The standard theory for ballistic transport suggests that, if specularity  
182 parameter  $p$  is zero,  $\Delta R$  emerges when the carrier mean free path in the bulk region becomes  
183 comparable to the sample width  $W$  [16]. If we assume that the charge carrier scattering in  
184 the bulk region is dominated by long-range scattering, the emergence of  $\Delta R$  at  $l_{\text{long}} \sim 1 \mu\text{m}$   
185 indicates the almost zero  $p$  in our device.

186 In summary, we conducted magnetotransport measurements in quasi-ballistic graphene/hexagonal  
187 boron nitride mesoscopic wires, in which the carrier mean free path is comparable to the wire  
188 width. Magnetoresistance curves show characteristic peak structures where the peak field  
189 scales with the ratio of cyclotron radius  $R_c$  and electronic wire width  $W$ , which indicates the  
190 detection of a diffusive scattering effect at the sample boundary. The analysis suggests that  
191 the values of  $R_c$  and  $W$  scale as  $R_c/W = 0.9 \pm 0.1$ . This is in contrast to the semiconductor  
192 two-dimensional electron system where  $R_c/W = 0.55$ . The analysis also suggests nearly zero  
193 probability for specular scattering at the sample boundary. These findings are fundamental  
194 step forward in understanding the effects of boundary scattering on the transport properties  
195 of nanostructured graphene devices such as graphene nanoribbons [35] and graphene single  
196 electron transistors [36, 37].

197 The authors acknowledge R. Moriya, S. Morikawa, K. Takase, and K. Muraki for technical  
198 support and helpful discussions. This study was supported by the PRESTO, Japan Science  
199 and Technology agency, the Grants-in-Aid from the MEXT, the CREST, Japan Science and  
200 Technology Agency, and the Project for Developing Innovation Systems of the MEXT.

- 
- 201 \* msatoru@iis.u-tokyo.ac.jp  
202 † tmachida@iis.u-tokyo.ac.jp
- 203 [1] K. S. Novoselov, A. K. Geim, S. V. Morozov, D. Jiang, Y. Zhang, S. V. Dubonos, I. V.  
204 Grigorieva, A. A. Firsov, *Science* **306**, 666 (2004).
- 205 [2] K. S. Novoselov, A. K. Geim, S. V. Morozov, D. Jiang, M. I. Katsnelson, I. V. Grigorieva, S.  
206 V. Dubonos, and A. A. Firsov, *Nature* **438**, 197 (2005).
- 207 [3] Y. Zhang, Y-W. Tan, H. L. Stormer, and P. Kim, *Nature* **438**, 201 (2005).
- 208 [4] Xu Du, I. Skachko, F. Duerr, A. Luican, and E. Y. Andrei, *Nature* **462**, 192 (2009).
- 209 [5] K. I. Bolotin, F. Ghahari, M. D. Shulman, H. L. Stormer, and P. Kim, *Nature* **462**, 196 (2009).
- 210 [6] C. W. J. Beenakker, and H. van Houten, in *Solid State Physics*, edited by E. Henry, and T.  
211 David (Academic Press, 1991), pp. 1.
- 212 [7] A. F. Young, and P. Kim, *Nature Physics* **5**, 222 (2009).
- 213 [8] J. Tworzydło, B. Trauzettel, M. Titov, A. Rycerz, and C. W. J. Beenakker, *Phys. Rev. Lett.*  
214 **96**, 246802 (2006).
- 215 [9] R. Danneau, F. Wu, M. F. Craciun, S. Russo, M. Y. Tomi, J. Salmilehto, A. F. Morpurgo,  
216 and P. J. Hakonen, *Phys. Rev. Lett.* **100**, 196802 (2008).
- 217 [10] J.-H. Chen, C. Jang, S. Adam, M. S. Fuhrer, E. D. Williams, and M. Ishigami, *Nature Physics*  
218 **4**, 377 (2008).
- 219 [11] J.-H. Chen, W. G. Cullen, C. Jang, M. S. Fuhrer, and E. D. Williams, *Phys. Rev. Lett.* **102**,  
220 236805 (2009).
- 221 [12] J.-H. Chen, C. Jang, S. Xiao, M. Ishigami, and M. S. Fuhrer, *Nature Nanotechnology* **3**, 206  
222 (2008).
- 223 [13] E. H. Hwang, and S. Das Sarma, *Phys. Rev. B* **77**, 115449 (2008).
- 224 [14] S. Fratini, and F. Guinea, *Phys. Rev. B* **77**, 195415 (2008).
- 225 [15] E. V. Castro, H. Ochoa, M. I. Katsnelson, R. V. Gorbachev, D. C. Elias, K. S. Novoselov, A.  
226 K. Geim, and F. Guinea, *Phys. Rev. Lett.* **105**, 266601 (2010).
- 227 [16] T. J. Thornton, M. L. Roukes, A. Scherer, and B. P. Van de Gaag, *Phys. Rev. Lett.* **63**, 2128  
228 (1989).
- 229 [17] R. Held, S. Lüscher, T. Heinzel, K. Ensslin, and W. Wegscheider, *Appl. Phys. Lett.* **75**, 1134

- 230 (1999).
- 231 [18] Y. Tokura, and S. Tarucha, Phys. Rev. B **55**, 15740 (1997).
- 232 [19] H. Akera, and T. Ando, Phys. Rev. B **43**, 11676 (1991).
- 233 [20] C. R. Dean, A. F. Young, I. Meric, C. Lee, L. Wang, S. Sorgenfrei, K. Watanabe, T. Taniguchi,  
234 P. Kim, K. L. Shepard, and J. Hone, Nature Nanotechnology **5**, 722 (2010).
- 235 [21] K. Watanabe, T. Taniguchi, and H. Kanda, Nature Materials **3**, 404 (2004).
- 236 [22] A. S. Mayorov, R. V. Gorbachev, S. V. Morozov, L. Britnell, R. Jalil, L. A. Ponomarenko, P.  
237 Blake, K. S. Novoselov, K. Watanabe, T. Taniguchi, and A. K. Geim, Nano Lett. **11**, 2396  
238 (2011).
- 239 [23] This value was calculated for typical charge carrier concentration  $n \sim 10^{12} \text{ cm}^{-2}$
- 240 [24] X. Du, I. Skachko, A. Barker, and E. Y. Andrei, Nature Nanotechnology **3**, 491 (2008).
- 241 [25] K. I. Bolotin, K. J. Sikes, J. Hone, H. L. Stormer, and P. Kim, Phys. Rev. Lett. **101**, 096802  
242 (2008).
- 243 [26] The absence of boundary scattering effect in suspended graphene might be due to limited  
244 channel length of suspended graphene.
- 245 [27] S. Masubuchi, M. Arai, and T. Machida, Nano Lett. **11**, 4542 (2011).
- 246 [28] S. Masubuchi, M. Ono, K. Yoshida, K. Hirakawa, and T. Machida, Appl. Phys. Lett. **94**,  
247 082107 (2009).
- 248 [29] S. Masubuchi, K. Suga, M. Ono, K. Kindo, S. Takeyama, and T. Machida, J. Phys. Soc. Jpn.  
249 **77**, 113707 (2008).
- 250 [30] E. H. Hwang, S. Adam, and S. Das Sarma, Phys. Rev. Lett. **98**, 186806 (2007).
- 251 [31] S. Das Sarma, S. Adam, E. H. Hwang, E. Rossi, Rev. Mod. Phys. **83**, 407 (2011).
- 252 [32] In our measurements, the magnetic field range studied was much larger than the field range  
253 where weak localization takes place  $B < 100 \text{ mT}$ . Therefore, we consider that the contribution  
254 of weak localization needs not be concerned in this work.
- 255 [33] P. Rakyta, A. Kormányos, J. Cserti, and P. Koskinen, Phys. Rev. B **81**, 115411 (2010).
- 256 [34] T. H. H. Xu, and I. V. Zozoulenko, Eur. Phys. Lett. **98**, 28808 (2012).
- 257 [35] M. Y. Han, B. Özyilmaz, Y. Zhang, and P. Kim, Phys. Rev. Lett. **98**, 206805 (2007).
- 258 [36] L. A. Ponomarenko, F. Schedin, M. I. Katsnelson, R. Yang, E. W. Hill, K. S. Novoselov, A.  
259 K. Geim, Science **320**, 356 (2008).
- 260 [37] C. Stampfer, J. Güttinger, F. Molitor, D. Graf, T. Ihn, and K. Ensslin, Appl. Phys. Lett. **92**,



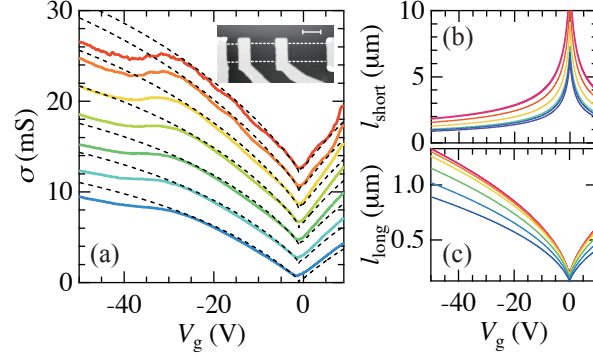


FIG. 1. (Color online) (a) Conductivity  $\sigma$  as a function of back-gate bias voltage  $V_g$  measured at  $T = 4, 16, 60, 120, 180, 240,$  and  $300$  K (top to bottom). For clarity, each curve was offset by 2 mS. Dashed curves are the calculated conductivity based on the Boltzmann equation discussed in the main text. The inset shows the atomic force microscopy image of the GBN sample studied in this work. The white region indicates the region of Pd metal electrodes. The white dashed lines indicate the outline of the graphene flake. (b) Short-range mean free path  $l_{\text{short}}$  and (c) long-range mean free path  $l_{\text{long}}$  as a function of gate-bias voltage  $V_g$ , for  $T = 4, 16, 60, 120, 180, 240,$  and  $300$  K (top to bottom).

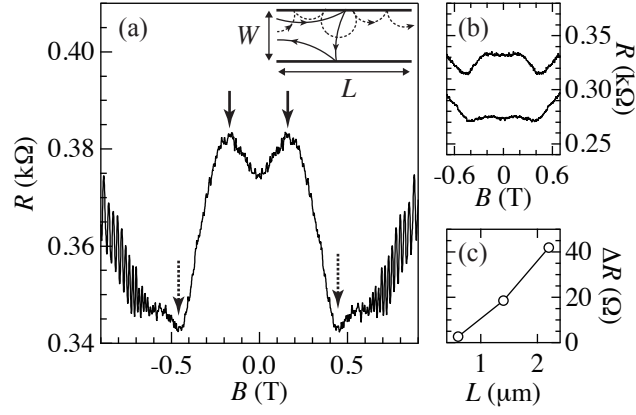


FIG. 2. (a) Two-terminal resistance  $R$  as a function of  $B$  measured at  $T = 4$  K for the device with channel length  $L = 2.3 \mu\text{m}$  with applied gate-bias voltage  $V_g = -45.0$  V. (inset) The schematic of electro-trajectories in mesoscopic wire for (solid curve)  $R_c > W$  and (dotted curve)  $R_c < W$ . (b)  $R$  as a function of  $B$  measured at  $T = 4$  K for (top curve)  $L = 1.4 \mu\text{m}$  and (bottom curve)  $L = 0.6 \mu\text{m}$ . (c) The amplitude of magnetoresistance signal  $\Delta R$  vs. channel length  $L$ .

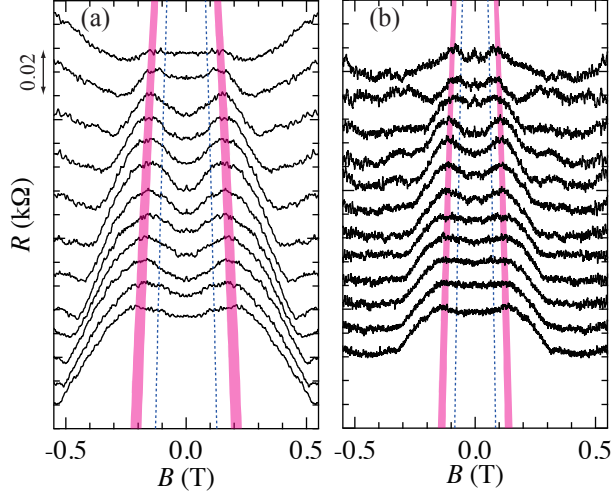


FIG. 3. (Color online) (a)  $R$  as a function of  $B$  measured at  $T =$  (a) 4 and (b) 1.6 K for the device with  $(L, W) =$  (a)  $(2.3 \mu\text{m}, 1.0 \mu\text{m})$  and (b)  $(3.1 \mu\text{m}, 1.5 \mu\text{m})$  with applied gate-bias voltage  $V_g = -50, -48, \dots, -28$  V (bottom to top). Each curve was offset vertically so that peak positions were separated by  $0.01 \text{ k}\Omega$ . The blue dotted curves and colored area indicate the expected peak positions for  $\alpha = 0.55$  and  $0.9 \pm 0.1$  respectively.

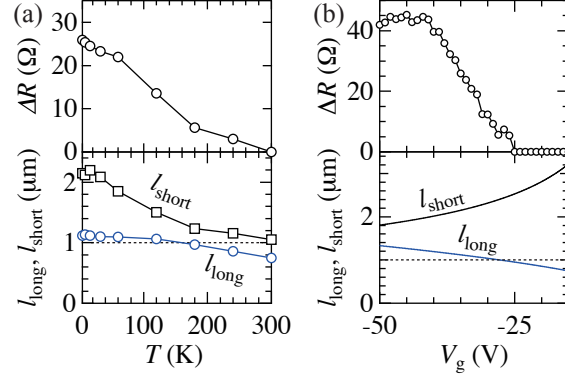


FIG. 4. (a)  $\Delta R$  (top panel),  $l_{\text{long}}$  (blue curve in bottom panel), and  $l_{\text{short}}$  (black curve in bottom panel) as a function of  $T$  measured in the device with channel length  $L = 2.3 \mu\text{m}$  at  $V_g = -35 \text{ V}$ . (b)  $\Delta R$  (top panel),  $l_{\text{long}}$  (blue curve in bottom panel), and  $l_{\text{short}}$  (black curve in bottom panel) as a function of  $V_g$  at  $T = 4 \text{ K}$ . The dotted line is the channel width of GBN mesoscopic wire.